Outage Performance with Deep Learning Analysis for UAV-Borne IRS Relaying NOMA Systems with Hardware Impairments

Chandan Kumar Singh[1], Prabhat Kumar Upadhyay[1,2], Janne Lehtomäki[2], and Markku Juntti[2]
[1]Department of Electrical Engineering, Indian Institute of Technology Indore, Indore 453552, Madhya Pradesh, India
[2]Centre for Wireless Communications (CWC), University of Oulu, 90014 Oulu, Finland
Email: phd1801202003@iiti.ac.in, pkupadhyay@iiti.ac.in, janne.lehtomaki@oulu.fi, markku.juntti@oulu.fi)

***Abstract*—While intelligent reflecting surfaces (IRSs) and non-orthogonal multiple access (NOMA) techniques have shown great potential to boost the spectral and energy efficiency for future wireless networks, unmanned aerial vehicles (UAVs) are committed for enhancing the wireless connectivity with fast and flexible deployment. In this regard, we study an integration of an IRS in UAV-enabled wireless relaying system using NOMA transmissions. We also count on the impacts of residual hardware impairments (HIs) in user devices and imperfect successive interference cancellation (SIC) in NOMA, which are inevitable in practical system implementation. We analyze the system performance by deriving the closed-form expressions of outage probability (OP) and system throughput over the line-of-sight (LoS) Rician fading channels for the aerial links. We further pursue asymptotic OP analysis to reveal useful insights on the achievable diversity order. Above all, we present a deep neural network (DNN) framework for OP prediction with a short execution time under the dynamic stochastic environment. Our results validate the theoretical proposition and accentuate the performance advantages of the proposed UAV-borne IRS relaying NOMA system.**

***Index Terms*—Deep neural network (DNN), intelligent reflecting surface (IRS), non-orthogonal multiple access (NOMA), outage probability, unmanned aerial vehicle (UAV).**

I. Introduction

Intelligent reflecting surfaces (IRSs) are proliferating as a revolutionary technology for the sixth generation (6G) wireless networks, owing to their potential to intelligently reconfigure radio propagation environment with a low-cost implementation [1], [2]. An IRS is equipped with multiple passive reflective elements that can be controlled by software to provide reflecting paths for radio communication signals in the desirable directions. Thereby, the IRS can achieve reduced energy consumption and efficient spectrum utilization in contrast to the traditional cooperative relaying technique [3]. Various research works have been conducted on the performance analysis of IRS-assisted transmission in order to take cognizance of the relaying operation (see [4], [5] and the references cited therein).

On the other hand, non-orthogonal multiple access (NOMA) has been emerged as a promising technology that enables multiple users to share the same code, time and spectrum resources [6]. Basically, it applies superposition coding in the power domain at the transmitter and successive interference cancellation (SIC) at the receiver to serve the multiple users. A series of research works have elucidated that the integration of NOMA with IRS can boost the spectral and energy efficiency for future wireless networks. A comparative performance investigation of NOMA over orthogonal multiple access (OMA) in the IRS-aided downlink communication system has been conducted in [7]. Authors in [8] have studied the performance of an IRS-NOMA system using coherent and random discrete phase shifting methods. An IRS-assisted NOMA networks with imperfect SIC has been analyzed in [9] by exploiting 1-bit coding scheme. The IRS is employed with millimeter wave NOMA communications in [10] and with wireless powered NOMA Internet-of-Things (IoT) networks in [11]. Considering an IRS-assisted NOMA downlink communication system, deep learning and reinforcement learning approaches have been applied for the optimization of NOMA user partitioning and IRS phase shifting in [12], and for the performance investigation over fading channels in [13].

The aforementioned research works considered the IRS transmissions in anticipation with fixed relaying infrastructure. An unmanned aerial vehicle (UAV) can facilitate flexible relaying through aerial domain to extend the coverage of base station, and provide on-demand services to the ground users by changing its location in real time. In addition, the UAV-based relaying establishes a spatial diversity path over and above the direct communication link between the transmitter and receiver. More importantly, a UAV-borne IRS system can proficiently subside the on-board UAV energy consumption by holding the UAV's transceiver in idle mode and allowing the IRS transmissions to serve the ground users. To this end, authors in [14] investigated the performance of an integrated UAV-IRS relaying for a single user system. The authors in [15] employed an IRS to improve the coverage performance between a mobile UAV and a ground user. In [16], authors have explored reinforcement learning for the optimization of the location of a UAV-IRS system so as to maximize the downlink transmission capacity. However, these research works did not consider NOMA transmissions with the UAV-mounted IRS relaying system. Further, in view of practical IoT implementation, the transmitter and receiver devices are built with low-cost hardware and hence liable to residual hardware impairments (HIs), which are attributed to partial

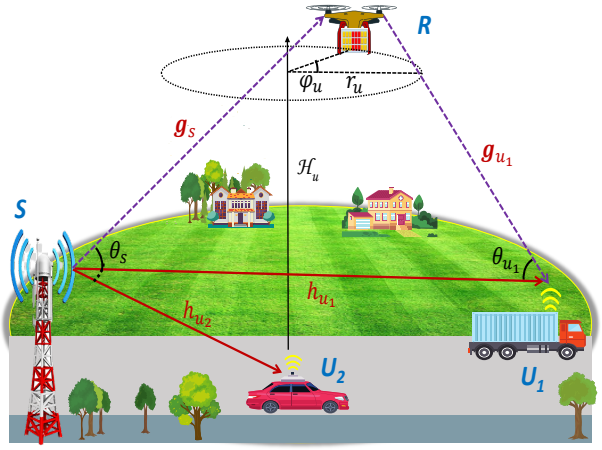

Fig. 1: A UAV-borne IRS relaying NOMA system.

compensation against several non-ideal factors such as in-quadrature-phase imbalance, amplifier nonlinearity, and phase noise [17], [18]. Also, the perfect SIC condition for the NOMA-based networks is quite difficult to realize in practice considering error propagation and complexity scaling. Note that the effects of residual HIs in user devices and imperfect SIC in NOMA may incur limitations on the capacity of the UAV-IRS relaying NOMA system, strikingly for the high rate applications.

Actuated by the above discussion, in this paper, we study a UAV-borne IRS relaying NOMA system under the influence of residual HIs and imperfect SIC. As the UAV-IRS is usually deployed in a position with line-of-sight (LoS) to both transmitter and receiver, we adopt the Rician fading model coupled with UAV propagation characteristics for the aerial channels and non-LoS Rayleigh fading for the terrestrial channels. We analyze the system performance by deriving closed-form expressions for outage probability (OP) of NOMA users and system throughput. We also pursue an asymptotic OP analysis to reveal the impact of key parameters on the system performance. Recognizing the complexity in derivations of OP metrics, we prosper a deep neural network (DNN) framework for OP prediction with low computational complexity and short execution time, with the goal of realizing a real-time UAV-IRS relaying NOMA network configuration.

II. System Model

Fig. 1 shows a UAV-borne IRS relaying system, where source (S) communicates with two NOMA users (U_1 and U_2) with the assistance of a UAV-IRS relay (R). As we consider U_1 as the far user and U_2 as the near user, the user U_1 receives signal transmitted from source via direct link as well as via UAV-IRS relay link, while the user U_2 receives the signal from source via direct link only. There is no communication link between the R and U_2 due to relatively weaker path [8] and blocking obstacles. The source and the users are equipped with a single antenna. The IRS is mounted on the UAV and is equipped with N reconfigurable reflecting elements whose phase shifts can be intelligently adjusted through a controller [8], [9] to maximize the received signal power at the user U_1. The $N \times N$ diagonal phase-shifting matrix at the IRS is given by

$$\mathbf{\Phi} = \text{diag}\left(\beta_1 e^{j\phi_1},\, \beta_2 e^{j\phi_2}, ...,\, \beta_N e^{j\phi_N}\right), \tag{1}$$

where $\beta_n \in (0, 1]$ is the nth amplitude-reflection coefficient, with $\beta_n = 1$ implies lossless reflection, and $\phi_n \in [0, 2\pi)$ is the nth phase-shift variable.

With three-dimensional (3-D) Cartesian coordinates, the locations of ground nodes S, U_1, and U_2 are represented by $\mathbf{v}_s = (\mathcal{X}_s, \mathcal{Y}_s, 0)$, $\mathbf{v}_{u_1} = (\mathcal{X}_{u_1}, \mathcal{Y}_{u_1}, 0)$, and $\mathbf{v}_{u_2} = (\mathcal{X}_{u_2}, \mathcal{Y}_{u_2}, 0)$, respectively. It is assumed that the UAV will travel in a circular trajectory with radius r_u, at height $\mathcal{H}_u$ such that $\mathcal{H}_u \in [\mathcal{H}_u^{\min}, \mathcal{H}_u^{\max}]$, and constant velocity, where $\mathcal{H}_u^{\min}$ and $\mathcal{H}_u^{\max}$ are the lowest and highest permissible altitudes, respectively. Let φ_u be the angle at which the UAV is now located within the UAV circle with reference to x-axis. Consequently, $\mathbf{v}_u = (r_u \cos\varphi_u,\, r_u \sin\varphi_u,\, \mathcal{H}_u)$ can be used to represent the location of the UAV. With two-dimensional (2-D) Cartesian coordinates, the location of $S, U_i, i \in \{1, 2\}$, and the UAV can be represented as $\mathbf{w}_s = (\mathcal{X}_s, \mathcal{Y}_s)$, $\mathbf{w}_{u_i} = (\mathcal{X}_{u_i}, \mathcal{Y}_{u_i})$, and $\mathbf{w}_u = (r_u \cos\varphi_u,\, r_u \sin\varphi_u)$, respectively. The elevation angles (in rad) from ground nodes S and U_1 are given by $\theta_s = \arctan\left(\frac{\mathcal{H}_u}{|\mathbf{w}_u - \mathbf{w}_s|}\right)$ and $\theta_{u_1} = \arctan\left(\frac{\mathcal{H}_u}{|\mathbf{w}_u - \mathbf{w}_{u_1}|}\right)$, respectively.

A. Channel Model

The communication links between the UAV and ground nodes (S and U_1) may have LoS or non-LoS depending upon the elevation angle and environment. Thus, the probability of LoS in their pertinent links is given by

$$P_L(\theta_j) = \Big(1 + \varepsilon_j \exp\big(-\xi_j(\theta_j - \varepsilon_j)\big)\Big)^{-1}, \tag{2}$$

where ε_j and ξ_j, with $j \in \{s, u_1\}$, denote the environment parameters fetched from the curve fitting using Damped Least-Squares (DLS) method [19]. The corresponding path-loss exponent is given by

$$\alpha_{r,j}(\theta_j) = P_L(\theta_j)\kappa_j + \nu_j, \tag{3}$$

where κ_j and ν_j, with $j \in \{s, u_1\}$, represent constants that depend on the uplink and downlink environment [19]. Let us denote the $N \times 1$ aerial channel vector between the source and the UAV-IRS by $\mathbf{g}_s$ and that between the UAV-IRS and user U_1 by $\mathbf{g}_{u_1}$. Since the UAV-IRS is usually deployed at a location that has LoS to both S and U_1, it is enviable to adopt Rician fading model for $\mathbf{g}_s$ and $\mathbf{g}_{u_1}$ as

$$\mathbf{g}_j = \sqrt{\frac{K_j}{K_j + 1}}\bar{\mathbf{g}}_j + \sqrt{\frac{1}{K_j + 1}}\tilde{\mathbf{g}}_j, \text{ for } j \in \{s, u_1\}, \tag{4}$$

where K_j denotes the Rician factor, $\bar{\mathbf{g}}_j$ and $\tilde{\mathbf{g}}_j$ represent the normalized LoS and non-LoS components, respectively. We further assume Ω_j be the average power of the corresponding Rician channel gain, for $j \in \{s, u_1\}$. The distance of the link between S and R is $d_{sr} = \sqrt{|\mathbf{w}_u - \mathbf{w}_s|^2 + \mathcal{H}_u^2}$ and that between R and U_1 is $d_{ru_1} = \sqrt{|\mathbf{w}_u - \mathbf{w}_{u_1}|^2 + \mathcal{H}_u^2}$, and

the corresponding aerial path-loss exponents are $\alpha_{r,s}(\theta_s)$ and $\alpha_{r,u_1}(\theta_{u_1})$.

On the contrary, as there is no LoS path between source S and user U_i, we assume that the terrestrial channel coefficient h_{u_i} between S and U_i, modelled as $\mathcal{CN}(0,\Omega_{su_i})$, for $i \in \{1,2\}$, undergoes Rayleigh fading. Also, we consider that $d_{su_i} = |\mathbf{w}_s - \mathbf{w}_{u_i}|^2$ and α_{su_i} be the distance and path-loss exponent of the corresponding terrestrial channel.

B. Signal Model

In the purview of NOMA, source S applies a superposition of the unit-power message signals x_1 and x_2 for the intended users U_1 and U_2, respectively, with corresponding power allocation factors as δ_1 and δ_2, satisfying $\delta_1 > \delta_2$ and $\delta_1 + \delta_2 = 1$. The source S then broadcasts the superimposed signal with its transmit power P_s. The signal received at U_1, via both direct and UAV-IRS relaying links, can be given by

$$y_{u_1} = \left(\frac{h_{u_1}}{\sqrt{d_{su_1}^{\alpha_{su_1}}}} + \frac{\mathbf{g}_{u_1}^H \mathbf{\Phi}\, \mathbf{g}_s}{\sqrt{d_{sr}^{\alpha_{r,s}(\theta_s)} d_{ru_1}^{\alpha_{r,u_1}(\theta_{u_1})}}} \right) \times (\sqrt{\delta_1 P_s} x_1 + \sqrt{\delta_2 P_s} x_2 + \eta_{ts}) + \eta_{ru_1} + \upsilon_{u_1}, \quad (5)$$

and the signal received at U_2, via the direct link only, can be given by

$$y_{u_2} = \frac{h_{u_2}}{\sqrt{d_{su_2}^{\alpha_{su_2}}}} (\sqrt{\delta_1 P_s} x_1 + \sqrt{\delta_2 P_s} x_2 + \eta_{ts}) + \eta_{ru_2} + \upsilon_{u_2}, \quad (6)$$

where υ_{u_1} and υ_{u_2} represent additive white Gaussian noise (AWGN) at the respective nodes, modeled as $\mathcal{CN}(0, N_0)$. Herein, $\eta_{ts} \sim \mathcal{CN}(0, \lambda_{ts}^2 P_s)$ denotes the distortion noise caused by HI at the transmitter section of source S, $\eta_{ru_1} \sim \mathcal{CN}\Big(0, \lambda_{ru_1}^2 P_s \Big| \frac{h_{u_1}}{\sqrt{d_{su_1}^{\alpha_{su_1}}}} + \frac{\mathbf{g}_{u_1}^H \mathbf{\Phi}\, \mathbf{g}_s}{\sqrt{d_{sr}^{\alpha_{r,s}(\theta_s)} d_{ru_1}^{\alpha_{r,u_1}(\theta_{u_1})}}} \Big|^2 \Big)$ and $\eta_{ru_2} \sim \mathcal{CN}\Big(0, \lambda_{ru_2}^2 P_s \frac{|h_{u_2}|^2}{d_{su_2}^{\alpha_{su_2}}}\Big)$ denote the distortion noises caused by HIs at the receiving nodes U_1 and U_2, respectively, with λ_{ts}, λ_{ru_1}, and λ_{ru_2} representing the levels of HIs that can be measured as error vector magnitudes (EVMs) [17].

Let us consider $\beta_n = \beta \,\forall\, n$ without loss of generality, and assume that $g_{s,n}$ and $g_{u_1,n}$ be the n-th elements of $\mathbf{g}_s$ and $\mathbf{g}_{u_1}$, respectively. Then, based on the perfect knowledge of the channel phases ψ_{u_1} of h_{u_1}, $\psi_{s,n}$ of $g_{s,n}$, and $\psi_{u_1,n}$ of $g_{u_1,n}$, the IRS can adjust its phase shifts ϕ_n as

$$\phi_n = -\psi_{u_1} + \psi_{s,n} + \psi_{u_1,n}, \quad (7)$$

so that the received signal at the user U_1 can be expressed as

$$y_{u_1} = e^{-j\psi_{u_1}} \left(a_1 |h_{u_1}| + b_1 \sum_{n=1}^{N} |g_{u_1,n}|\, |g_{s,n}| \right) \times (\sqrt{\delta_1 P_s} x_1 + \sqrt{\delta_2 P_s} x_2 + \eta_{ts}) + \eta_{ru_1} + \upsilon_{u_1}, \quad (8)$$

where $a_1 = 1/\sqrt{d_{su_1}^{\alpha_{su_1}}}$ and $b_1 = \beta/\sqrt{d_{sr}^{\alpha_{r,s}(\theta_s)} d_{ru_1}^{\alpha_{r,u_1}(\theta_{u_1})}}$. Capitalizing on the NOMA scheme, the far user U_1 detects its message x_1 by treating the near user's message x_2 as interference. Thus, the signal-to-interference-plus-noise ratio (SINR) at U_1 is given by

$$\gamma_{u_1,x_1} = \frac{\delta_1 \rho_s \Big(a_1 |h_{u_1}| + b_1 \sum_{n=1}^{N} |g_{u_1,n}|\, |g_{s,n}| \Big)^2}{(\delta_2 + \lambda_{su_1}^2) \rho_s \Big(a_1 |h_{u_1}| + b_1 \sum_{n=1}^{N} |g_{u_1,n}|\, |g_{s,n}| \Big)^2 + 1}, \quad (9)$$

where $\lambda_{su_1}^2 = \lambda_{ts}^2 + \lambda_{ru_1}^2$ elucidates the aggregate HI level at the user U_1 and $\rho_s = \frac{P_s}{N_0}$ denotes the transmit signal-to-noise ratio (SNR).

Whereas, at near user U_2, the signal x_1 of U_1 is decoded first, and the corresponding SINR is given by

$$\gamma_{u_2,x_1} = \frac{\delta_1 \rho_s a_2 |h_{u_2}|^2}{(\delta_2 + \lambda_{su_2}^2)\, \rho_s a_2 |h_{u_2}|^2 + 1}, \quad (10)$$

where $a_2 = 1/d_{su_2}^{\alpha_{su_2}}$ and $\lambda_{su_2}^2 = \lambda_{ts}^2 + \lambda_{ru_2}^2$ which captures the aggregate HI level at the user U_2. Then, after striking out the signal x_1 using SIC, U_2 decodes its own message x_2. Thus, the corresponding SINR is given by

$$\gamma_{u_2,x_2} = \frac{\delta_2 \rho_s a_2 |h_{u_2}|^2}{\delta_1 \rho_s a_2 |h_2|^2 + \lambda_{su_2}^2 \rho_s a_2 |h_{u_2}|^2 + 1}, \quad (11)$$

where $\hbar_2$ accounts for the imperfect SIC error, modelled as $\mathcal{CN}(0, \zeta\Omega_2)$. Herein, $\zeta \in (0,1]$ refers to the level of residual interference arising due to imperfect SIC, with $\zeta = 0$ corresponds to the perfect SIC case.

III. Performance Analysis

In this section, we first evaluate OP performance of the system, and then present an asymptotic OP analysis to disclose useful insights. We also analyze a system throughput measure.

A. OP Evaluation

The OP is evaluated as the probability that the SINR falls below a predefined outage threshold.

1) OP for User U_1: Using (9), the OP for U_1 can be evaluated for a target rate R_{th_1} as

$$\mathcal{P}_{u_1} = \Pr\{\gamma_{u_1,x_1} < \gamma_{\text{th}_1}\} = \Pr\left\{ \left(a_1 |h_{u_1}| + b_1 \sum_{n=1}^{N} |g_{u_1,n}|\, |g_{s,n}| \right)^2 < \frac{\gamma_{\text{th}_1}}{\delta_1 \rho_s - (\delta_2 + \lambda_{su_1}^2) \rho_s \gamma_{\text{th}_1}} \right\}, \quad (12)$$

where $\gamma_{\text{th}_1} = 2^{R_{\text{th}_1}} - 1$. As the exact closed-form evaluation of $\mathcal{P}_{u_1}$ in (12) is intricate, we present a tight approximated expression in the following lemma.

Lemma 1: The OP $\mathcal{P}_{u_1}$ for the proposed UAV-IRS relaying NOMA system is given by

$$\mathcal{P}_{u_1} = \frac{1}{2} \left[1 + \text{erf}\left(\frac{\sqrt{w} - b_1 N \mu_1}{\sqrt{2 b_1^2 N \sigma_1^2}} \right) \right] - \frac{1}{2\sqrt{\tilde{c}_1}} e^{-\frac{(\sqrt{w} - b_1 N \mu_1)^2}{2 c_1}} \left[1 + \text{erf}\left(\frac{\sqrt{w} - b_1 N \mu_1}{\sqrt{2 b_1^2 N \sigma_1^2 \tilde{c}_1}} \right) \right], \quad (13)$$

for $\gamma_{\text{th}_1} < \frac{\delta_1}{\delta_2+\lambda_{su_1}^2}$, where $w = \frac{\gamma_{\text{th}_1}}{\delta_1 \rho_s - (\delta_2+\lambda_{su_1}^2)\rho_s\gamma_{\text{th}_1}}$, $\tilde{c}_1 = \frac{c_1}{a_1^2\Omega_{su_1}}$ with $c_1 = b_1^2 N\sigma_1^2 + a_1^2\Omega_{su_1}$, and

$$\mu_1 = \frac{\pi\sqrt{\Omega_s\Omega_{u_1}}}{2}\left[{}_1F_1\left(\frac{-1}{2};1;-K_s\right){}_1F_1\left(\frac{-1}{2};1;-K_{u_1}\right)\right],$$
$$\sigma_1^2 = 4\Omega_s\Omega_{u_1}(1+K_s)(1+K_{u_1}) - \frac{\pi^2\Omega_s\Omega_{u_1}}{4}\left[{}_1F_1\left(\frac{-1}{2};1;-K_s\right){}_1F_1\left(\frac{-1}{2};1;-K_{u_1}\right)\right]^2.$$

where ${}_1F_1(.)$ is the Confluent Hypergeometric function [20].

Proof: See Appendix A. ∎

Note that, for $\gamma_{\text{th}_1} \geq \frac{\delta_1}{\delta_2+\lambda_{su_1}^2}$, the $\mathcal{P}_{u_1}$ in (12) becomes unity and the user U_1 is said to suffer from a ceiling effect.

2) OP for User U_2: For a target rate R_{th_2}, the OP for U_2 can be evaluated as

$$\begin{aligned}\mathcal{P}_{u_2} &= \Pr\{\gamma_{u_2,x_1} < \gamma_{\text{th}_2} \text{ or } \gamma_{u_2,x_2} < \gamma_{\text{th}_2}\} \\ &= 1 - \Pr\{\gamma_{u_2,x_1} > \gamma_{\text{th}_2},\, \gamma_{u_2,x_2} > \gamma_{\text{th}_2}\}, \end{aligned} \quad (14)$$

where $\gamma_{\text{th}_2} = 2^{R_{\text{th}_2}}$. We proficiently solve (29) to present the result in the following lemma.

Lemma 2: The OP $\mathcal{P}_{u_2}$ for the proposed UAV-IRS relaying NOMA system is given by

$$\mathcal{P}_{u_2} = 1 - e^{-\frac{w_{22}}{2\Omega_{su_2}}}\left[1 - e^{-\frac{w_{21}-w_{22}}{w_{12}\zeta\Omega_2}}\right] - \frac{1}{\zeta\Omega_2}\left(\frac{w_{22}}{\Omega_{su_2}} + \frac{1}{\zeta\Omega_2}\right)^{-1} \times e^{-\frac{w_{22}}{2\Omega_{su_2}}} e^{-\left(\frac{w_{22}}{\Omega_{su_2}}+\frac{1}{\zeta\Omega_2}\right)\left(\frac{w_{21}-w_{22}}{w_{12}}\right)}, \quad (15)$$

for $\gamma_{\text{th}_2} < \frac{\delta_1}{\delta_2+\lambda_{su_2}^2}$, where $w_{21} = \frac{\gamma_{\text{th}_2}}{\delta_1 a_2\rho_s - (\delta_2+\lambda_{su_2}^2)a_2\rho_s\gamma_{\text{th}_2}}$, $w_{12} = \frac{\delta_1\gamma_{\text{th}_2}}{\delta_2-\lambda_{su_2}^2\gamma_{\text{th}_2}}$, and $w_{22} = \frac{\gamma_{\text{th}_2}}{\delta_2 a_2\rho_s - \lambda_{su_2}^2 a_2\rho_s\gamma_{\text{th}_2}}$.

Proof: See Appendix B. ∎

For $\gamma_{\text{th}_2} > \frac{\delta_1}{\delta_2+\lambda_{su_2}^2}$, $\mathcal{P}_{u_2}$ attains unity, implying the ceiling effect.

B. Asymptotic OP Evaluation

To extract more insights, we examine the asymptotic OP behavior of each user at high SNR ($\rho_s \to \infty$). For the case of user U_1, we apply the inequality $(u+v)^2 \geq u^2+v^2$ in (12) and solve the convoluted probability term to obtain

$$\mathcal{P}_{u_1} \simeq \frac{1}{\Gamma(\mathcal{A}+1)}\left(\frac{1}{\mathcal{A}+1}\right)\left(\frac{1}{b_1\mathcal{B}}\right)^{\mathcal{A}+1}\sum_{m=0}^{\frac{\mathcal{A}+1}{2}}\binom{\frac{\mathcal{A}+1}{2}}{m}(-1)^m \times \left(\frac{w_{11}}{\rho_s}\right)^{\frac{\mathcal{A}+1}{2}-m}\left(\frac{1}{a_1^2\Omega_{su_1}}\right)^{-m}\Upsilon\left(m+1, \frac{w_{11}}{\rho_s a_1^2\Omega_{su_1}}\right), \quad (16)$$

where $w_{11} = \frac{\gamma_{\text{th}_1}}{\delta_1 - (\delta_2+\lambda_{su_1}^2)\gamma_{\text{th}_1}}$, $\mathcal{A} = \frac{N\mu_1^2}{\sigma_1^2} - 1$, $\mathcal{B} = \frac{\sigma_1^2}{\mu_1}$, $\Gamma(\cdot)$ and $\Upsilon(\cdot,\cdot)$ denote the complete Gamma function and lower incomplete Gamma function, respectively. Further, applying the fact that $\Upsilon(\alpha,x) \underset{x\to 0}{\simeq} \frac{x^\alpha}{\alpha}$ and considering the first term in the series in (16) as the dominant term at $\rho_s \to \infty$, we obtain

$$\mathcal{P}_{u_1} \simeq \frac{1}{\Gamma(\mathcal{A}+1)}\left(\frac{1}{\mathcal{A}+1}\right)\left(\frac{1}{b_1\mathcal{B}}\right)^{\mathcal{A}+1}\frac{1}{a_1^2\Omega_{su_1}}\left(\frac{w_{11}}{\rho_s}\right)^{\frac{\mathcal{A}+3}{2}}. \quad (17)$$

From (17), one can infer that the achievable diversity order for user U_1 is $\frac{\mathcal{A}+3}{2} = \frac{N\mu_1^2}{2\sigma_1^2} + 1$. It depends on the number of reflecting elements of IRS and the Rician fading parameters. For the user U_2, we apply the approximation $e^{-x} \underset{x\to 0}{\simeq} 1-x$ in (15) to get the asymptotic behavior of $\mathcal{P}_{u_2}$ at high SNR as

$$\mathcal{P}_{u_2} \simeq 1 - \left(\frac{w_{21}-w_{22}}{w_{12}\zeta\Omega_2}\right)\left(1+\frac{w_{21}}{\Omega_{su_2}}\right) - \frac{1}{\zeta\Omega_2}\left(\frac{w_{12}}{\Omega_{su_2}}+\frac{1}{\zeta\Omega_2}\right)^{-1} \times \left(1-\frac{w_{22}}{\Omega_{su_2}}\right)\left[1-\left(\frac{w_{12}}{\Omega_{su_2}}+\frac{1}{\zeta\Omega_2}\right)\left(\frac{w_{21}-w_{22}}{w_{12}}\right)\right]. \quad (18)$$

It can be inferred from (18) that U_2 attains no diversity gain.

C. System Throughput

The system throughput infers the average spectral efficiency for the proposed UAV-IRS relaying NOMA system. It can be quantified as the sum of individual target rates for both users U_1 and U_2 that can be achieved successfully over the considered fading channels. From the derived OP expressions, system throughput can be formulated as

$$\mathcal{S}_\mathcal{T} = (1-\mathcal{P}_{u_1})\,R_{\text{th}_1} + (1-\mathcal{P}_{u_2})\,R_{\text{th}_2}. \quad (19)$$

Letting $R_{\text{th}_1} = R_{\text{th}_2} = \mathfrak{R}$ in (19), we get $2\mathfrak{R}$ as the maximum achievable system throughput which could be attained under ideal system conditions, when each user's OP goes to zero.

IV. Deep Neural Network Design

To overcome the difficulty and time consumption of mathematical analysis and Monte Carlo simulations, this section offers the DNN framework for estimating the OP with little computational complexity and quick run time.

A. Method for Generating Datasets

The OP functions in (12) and (14) are used to build the dataset for this study since they are connected to the system parameters like SNR ($\rho_s \in [0,60]$), target rate ($R_{\text{th}_1} = R_{\text{th}_2} \in [0.1,1]$), HIs level ($\lambda_{ts} = \lambda_{ru_1} = \lambda_{ru_2} = \lambda_0 \in [0,0.4]$), power factor ($\delta_1 \in [0.51,0.99]$), level of residual interference ($\zeta \in [0,0.5]$), and reflecting elements ($N \in [1,20]$). Based on the network size, each system parameter is created uniformly and used as an input variable for a training sample. The generated dataset $\mathcal{D}$ contains 10×10^5 samples in total, of which 80% are used for training ($\mathcal{D}_{trn}$) and the remaining 20% are equally divided between validation ($\mathcal{D}_{val}$) and testing ($\mathcal{D}_{tes}$). We have realized that in the majority of cases, this number of samples is sufficient to obtain quite accurate estimates.

B. Learning Model for DNN

A typical DNN is a feed-forward neural network with one input layer, numerous hidden layers, and one output layer. The six neurons in the input layer correspond to the six parameters provided in Section IV-A. For each input parameter m at each hidden layer, a threshold operation is carried out using an exponential linear unit (eLU) activation function. Any value below zero is scaled up to zero. Here is an illustration of how eLU functions:

$$\text{eLU}(m) = \begin{cases} \varpi\,(e^m - 1), & \text{if } m < 0, \\ m, & \text{if } m \geq 0, \end{cases} \quad (20)$$

where ϖ is a constant with the value 1. The eLU activation function has a number of advantages over the other activation functions because it has a near-linear form. The output layer just has one neuron because the regression problem predicts numerical values directly, without any later modification or activation function. We consider a layer that is completely connected, where the activation $\mathcal{F}_q^p$ of the q-th neuron in the p-th layer is coupled to activation in the $(p-1)$-th layer as

$$\mathcal{F}_q^p = \text{eLU}\left(\sum_{i=1}^{\mathcal{U}_{p-1}} \mathcal{W}_{q,i}^p \, \mathcal{F}_i^{p-1} + \mathcal{C}_q^p\right), \tag{21}$$

where $\mathcal{U}_{p-1}$ is the $(p-1)$-th layer's total number of neurons. The weight that links to the (i)-th neuron is denoted by $\mathcal{W}_{q,i}^p$ in the $(p-1)$-th layer, while a scalar bias is denoted by $\mathcal{C}_q^p$ in the (p)-th layer.

C. OP Real-Time Prediction

The DL architecture includes two stages: training and prediction. The adaptive moment estimation (Adam) optimization strategy, which tries to optimise set of parameters based on the dataset, is used to train the neural network offline while learning input-output correlations. Adam is used to compute/update the DNN model's weights and biases during the backpropagation process. Let $\mathcal{M}^d$ and $\bar{\mathcal{M}}^d$ reflect the actual and expected output values for the (d)-th testing datasets of the DNN model. The following loss function can be used to compute the mean-square error (MSE) between estimated and predicted values:

$$\text{Loss}\big(\mathcal{M}^d, \bar{\mathcal{M}}^d\big) = \frac{1}{\mathcal{D}_{tes}} \sum_{d=1}^{\mathcal{D}_{tes}} \big(\mathcal{M}^d - \bar{\mathcal{M}}^d\big)^2. \tag{22}$$

The following formula is used to calculate RMSE:

$$\text{RMSE} = \sqrt{\frac{1}{\mathcal{D}_{tes}} \sum_{d=1}^{\mathcal{D}_{tes}} \big(\mathcal{M}^d - \bar{\mathcal{M}}^d\big)^2}, \tag{23}$$

where $\mathcal{D}_{tes}$ stands for the overall sample size in the test-set.

D. Complexity Analysis of DNN model

The suggested DNN model's computational complexity is measured in terms of floating-point operations (FLOPs) per second, which depends on the amount of weights and bias in the network. As a result, the estimated DNN model has roughly 91k $(91,801)$ parameters and 182k $(182,851)$ FLOPs.

In the next section, we exemplify the execution times for OP prediction through the DNN evaluation in contrast to the mathematical analysis and Monte Carlo simulation.

V. Numerical and Simulation Results

In order to verify our theoretical aspects, we conduct numerical analysis for the proposed UAV-IRS relaying NOMA system in this part as well as exploit Monte-Carlo simulations in MATLAB version R2022a. Unless otherwise provided, we set numerous system parameters as $r_u = 0.3$ km, $\varphi_u = \pi$, $\mathcal{H}_u = 0.1$ km, $\mathbf{v}_s = (-1, 0, 0)$ km, $\mathbf{v}_{u_1} = (1, 0, 0)$ km,

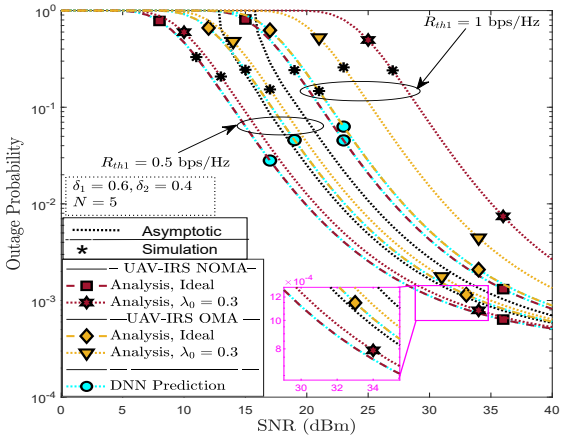

Fig. 2: OP performance of user U_1.

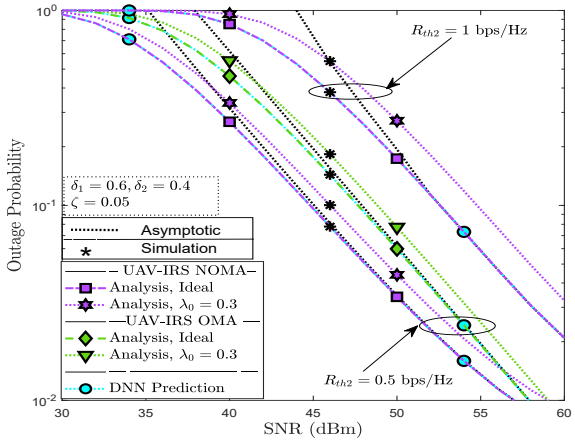

Fig. 3: OP performance of user U_2.

$\mathbf{v}_{u_2} = (0, -1, 0)$ km, $\Omega_s = \Omega_{u_1} = 0.5$, $\Omega_{su_1} = \Omega_{su_2} = 1$, $\Omega_2 = 0.1$, and $K_s = K_{u_1} = 1$. In addition, we take $\varepsilon_s = \varepsilon_{u_1} = 20$, $\xi_s = \xi_{u_1} = 0.5$, $\kappa_s = \kappa_{u_1} = -1.5$, $\nu_s = \nu_{u_1} = 3.5$, and $\alpha_{su_1} = \alpha_{su_2} = 2.5$ just like in [19] to validate the results that were produced. We also set $\lambda_{ts} = \lambda_{ru_1} = \lambda_{ru_2} = \lambda_0$ as the level of HIs such that $\lambda_{su_1} = \lambda_{su_2} = \sqrt{2}\lambda_0$, and $\beta = 1$ for the lossless reflection.

Python 3.7.13, in conjunction with Keras 2.8.0 and TensorFlow 2.8.0, are used to build a DNN model with four hidden layers and 150 hidden neurons per layer. The weights of the DNN are randomly initialized using the Adam optimizer and a gradient decay value of 0.95 during the duration of 70 epochs of training. It starts out with a learning rate of 10^{-3} (after 20 epochs fall 90%). A computer equipped with i7-7700 processor, GPU of 8 GB GeForce GTX 1080, and 16 GB of RAM was used for all of the testing.

Fig. 2 depicts the OP versus SNR curves for user U_1 using two different values of target rates i.e., $R_{\text{th}_1} = 0.5$ bps/Hz and $R_{\text{th}_1} = 1$ bps/Hz under both perfect (ideal) hardware $(\lambda_0 = 0)$ and the imperfect hardware $(\lambda_0 = 0.3)$. We select appropriate δ_1 and δ_2 values, complying with the condition as stated in Section III. In order to make comparisons, the OP curves are also provided for the UAV-IRS OMA-based relaying scheme. We can see that the analytical and simulated curves are tightly

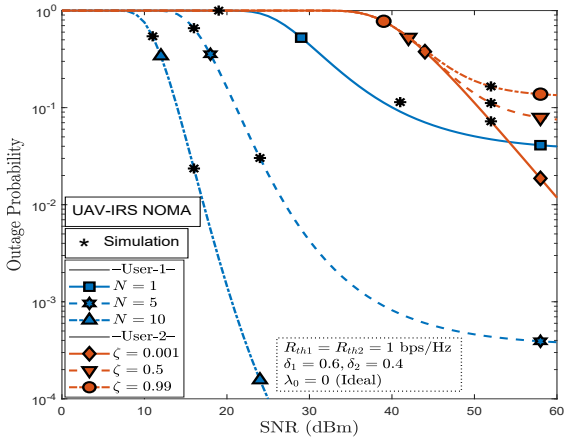

Fig. 4: Impact of N and ζ on users U_1 and U_2.

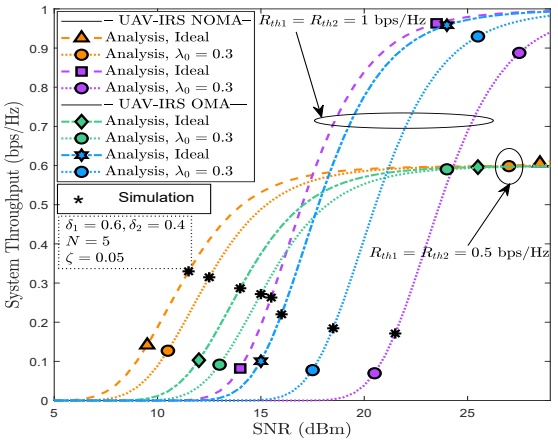

Fig. 5: System throughput versus SNR plots.

wedged over the operating SNR region. In the high SNR region, the asymptotic curves are also well aligned with the theoretical and simulated curves. Additionally, we can observe that for the fixed target rate, the UAV-IRS NOMA system outperforms the UAV-IRS OMA system. This is because the UAV-IRS OMA system needs two-time slots to complete its operation, and thereby the corresponding SINR threshold becomes higher than that for the NOMA counterpart (with the same target rate). We can also see that as the target rate increases, the U_1's performance suffers with the imposition of the HIs. Although the presence of HIs ($\lambda_0 = 0.3$) impairs the U_1's performance, its effects are more apparent at a higher target rate. It is important to observe that the HIs have a larger impact on the UAV-IRS NOMA system, which is more noticeable at the higher target rate. It is worthwhile to mention that the DNN prediction results are aligned with the simulation as well as the analytical formulation given in (13).

The OP performance of user U_2 is shown in Fig. 3 for the imperfect SIC case. Here, we vary the target rate as $R_{\text{th}_2} = 0.5, 1$ bps/Hz and the level of HIs as $\lambda_0 = 0, 0.3$. To start, it is possible to confirm that the simulated and analytical curves are perfectly aligned throughout the whole SNR region. In the high SNR region, the asymptotic curves are also well aligned with the theoretical and simulated curves. We can see from the plot that the UAV-IRS NOMA system performs better than the UAV-IRS OMA system for the fixed target rate. Additionally, the performance loss caused by HIs for UAV-IRS OMA system is less noticeable than that for UAV-IRS NOMA system. The results of the DNN predictions are accurately comparable to those of the analytical and simulation results, proving the superior prediction ability of the DNN.

We depict Fig. 4 by altering the values of N and ζ in order to thoroughly analyse the respective effects of the number of reflecting elements and imperfect SIC on the OP performance of users U_1 and U_2, respectively. As the values of the number of reflecting elements increase ($N = 1, 5$, and 10), the OP performance of U_1 becomes better. Also, as the level of imperfect SIC declines ($\zeta = 0.99, 0.5$, and 0.001), it is evident that the OP performance of U_2 considerably improves.

In order to get insight into the average spectral efficiency of the UAV-IRS relaying NOMA system, Fig. 5 highlights the system throughput curves based on the deduced analytical expression in Section III-C. Here, we plot the system throughput versus SNR for two different values of the target rate ($R_{\text{th}_1} = R_{\text{th}_2} = 0.5, 1$ bps/Hz). The relevant graphs show that, in the low SNR region, system throughput declines as the target rate rises. For the set target rate, however, the system throughput grows up to a specific SNR value before becoming saturated. For the specified target rate, this saturated level is referred to as the maximum throughput that can be achieved. For a higher value of the target rate, this throughput saturation occurs at a relatively high SNR. This is because outage performance at higher target rates is generally worse than outage performance at lower target rates. Additionally, one can observe that system throughput falls as the level of HIs arises from $\lambda_0 = 0$ to $\lambda_0 = 0.3$.

Above all, the DNN evaluation, mathematical analysis, and Monte Carlo simulation for the proposed system are contrasted in terms of execution times. The outcomes show that the DNN prediction method requires just 0.0197 seconds to obtain OP values. The mathematical evaluation takes 0.0406 seconds, whereas the Monte Carlo simulation needs 6.0927 seconds to obtain the OP values. The RMSE is determined as 0.0072 using the mathematical analysis and DNN prediction results.

VI. Conclusion

We have conducted outage performance evaluation and DNN analysis for a UAV-borne IRS relaying NOMA system under the impacts of transceiver HIs and imperfect SIC. The pertinent channel characteristics of the UAV/IRS-to-ground links with LoS Rician fading are explored to describe the system performance. The closed-form expressions for OP of NOMA users and system throughput are derived for performance evaluation. To acquire more understanding, asymptotic approximations in the high SNR regime are presented to determine the diversity order for each user. It is shown that the Rician fading parameters and the number of IRS reflecting elements have an impact on the diversity order. Numerical results illustrated that the UAV-IRS NOMA system

can perform better than its competitive OMA counterparts while accommodating non-ideal system imperfections like transceiver HIs and imperfect SIC. The DNN framework is created to counter the analytical complexity of OP evaluation and to predict the OP accurately with a short execution time.

APPENDIX A

Letting $X_1 = |h_{u_1}|$ and $Y_1 = \sum_{n=1}^{N} |g_{u_1,n}|\,|g_{s,n}|$, we can define $Z = a_1 X_1 + b_1 Y_1$, and hence express $\mathcal{P}_{u_1}$ in (24) as

$$\mathcal{P}_{u_1} = \Pr\{Z^2 < w\} = \Pr\{Z < \sqrt{w}\} = F_Z(\sqrt{w}). \quad (24)$$

Hereby, as X_1 follows Rayleigh distribution with parameter Ω_{su_1}, the probability density function (PDF) and cumulative distribution function (CDF) of X_1 are given, respectively, by

$$f_{X_1}(x) = \frac{x}{\Omega_{su_1}} e^{-\frac{x^2}{2\Omega_{su_1}}} \quad (25)$$

$$\text{and} \quad F_{X_1}(x) = 1 - e^{-\frac{x^2}{2\Omega_{su_1}}}. \quad (26)$$

Whereas, according to central limit theorem (CLT), Y_1 can be approximated as a Gaussian random variable i.e., $Y_1 \sim \mathcal{N}(N\mu_1, N\sigma_1^2)$, and hence, the PDF of Y_1 is given by

$$f_{Y_1}(y) = \frac{1}{\sqrt{2\pi N\sigma_1^2}} e^{-\frac{(y-N\mu_1)^2}{2N\sigma_1^2}}, \quad (27)$$

where $\mu_1 = \mathbb{E}\{|g_{u_1,n}|\,|g_{s,n}|\}$ and $\sigma_1^2 = \text{var}\{|g_{u_1,n}|\,|g_{s,n}|\}$ are deduced after (13). Now, we can evaluate the CDF of Z as

$$\begin{aligned} F_Z(z) &= \Pr\{Z < z\} = \Pr\{a_1 X_1 + b_1 Y_1 < z\} \\ &= \int_{-\infty}^{\frac{z}{b_1}} F_{X_1}\left(\frac{z}{a_1} - \frac{b_1}{a_1} y\right) f_{Y_1}(y) dy. \end{aligned} \quad (28)$$

On using (26) and (27) in (28) and solving the integral, we obtain the result which is applied in (24) to get (13).

APPENDIX B

On using (10) and (11), and doing some manipulations, we can further evaluate (14) as

$$\begin{aligned} \mathcal{P}_{u_2} &= 1 - \Pr\left\{|h_{u_2}|^2 > w_{21},\, |h_{u_2}|^2 > w_{12}|\hbar_2|^2 + w_{22}\right\} \\ &= 1 - \underbrace{\Pr\left\{|h_{u_2}|^2 > \max\{w_{21}, w_{12}|\hbar_2|^2 + w_{22}\}\right\}}_{\overline{\mathcal{P}}_{u_2}}, \end{aligned} \quad (29)$$

We can split the probability term $\overline{\mathcal{P}}_{u_2}$ into two parts to express $\overline{\mathcal{P}}_{u_2} = \mathcal{P}_{21} + \mathcal{P}_{22}$, where $\mathcal{P}_{21}$ and $\mathcal{P}_{22}$ are evaluated as

$$\begin{aligned} \mathcal{P}_{21} &= \Pr\left\{|h_{u_2}|^2 > w_{21},\, w_{21} > w_{12}|\hbar_2|^2 + w_{22}\right\} \\ &= \int_0^{\frac{w_{21}-w_{22}}{w_{12}}} \int_{w_{21}}^{\infty} f_{|h_{u_2}|^2}(x) f_{|\hbar_2|^2}(y) \end{aligned} \quad (30)$$

$$\begin{aligned} \mathcal{P}_{22} &= \Pr\left\{|h_{u_2}|^2 > w_{12}|\hbar_2|^2 + w_{22},\, w_{21} < w_{12}|\hbar_2|^2 + w_{22}\right\} \\ &= \int_{\frac{w_{21}-w_{22}}{w_{12}}}^{\infty} \int_{w_{12}y+w_{22}}^{\infty} f_{|h_{u_2}|^2}(x) f_{|\hbar_2|^2}(y). \end{aligned} \quad (31)$$

Under Rayleigh fading, $|h_{u_2}|^2$ and $|\hbar_2|^2$ follow exponential distributions with parameters Ω_{su_2} and $\zeta\Omega_2$, respectively. Thus, on inserting their PDFs into (30) and (31), solving the involved integrals, and inserting the obtained results for $\overline{\mathcal{P}}_{u_2}$ in (29), we reach at the OP expression as presented in (15).

ACKNOWLEDGMENTS

This research work is supported by the Nokia Foundation Visiting Professor Grant and the Visvesvaraya PhD Scheme of Ministry of Electronics & Information Technology (MeitY), Government of India, being implemented by Digital India Corporation (formerly Media Lab Asia), and in part by the Academy of Finland 6Genesis Flagship under Grant 318927.

REFERENCES

[1] Q. Wu and R. Zhang, "Towards smart and reconfigurable environment: Intelligent reflecting surface aided wireless network," *IEEE Commun. Mag.*, vol. 58, no. 1, pp. 106–112, Jan. 2020.

[2] Y. Zhu, B. Mao, Y. Kawamoto, and N. Kato, "Intelligent reflecting surface-aided vehicular networks toward 6G: Vision, proposal, and future directions," *IEEE Veh. Technol. Mag.*, vol. 16, no. 4, pp. 2–10, Dec. 2021.

[3] E. Bjornson, Ö. Özdogan, and E. G. Larsson, "Intelligent reflecting surface versus decode-and-forward: How large surfaces are needed to beat relaying?," *IEEE Wireless Commun. Lett.*, vol. 9, no. 2, pp. 244–248, Feb. 2020.

[4] A. M. Salhab and M. H. Samuh, "Accurate performance analysis of reconfigurable intelligent surfaces over Rician fading channels," *IEEE Wireless Commun. Lett.*, vol. 10, no. 5, pp. 1051-1055, May 2021.

[5] D. Selimis, K. P. Peppas, G. C. Alexandropoulos, and F. I. Lazarakis, "On the performance analysis of RIS-empowered communications over Nakagami-*m* fading," *IEEE Commun. Lett.*, vol. 25, no. 7, pp. 2191–2195, Jul. 2021.

[6] Z. Ding, P. Fan, and H. V. Poor, "Impact of user pairing on 5G nonorthogonal multiple-access downlink transmissions," *IEEE Trans. Veh. Technol.*, vol. 65, no. 8, pp. 6010–6023, Aug. 2016.

[7] B. Zheng, Q. Wu, and R. Zhang, "Intelligent reflecting surface-assisted multiple access with user pairing: NOMA or OMA?" *IEEE Commun. Lett.*, vol. 24, no. 4, pp. 753–757, Apr. 2020.

[8] Z. Ding, R. Schober, and H. V. Poor, "On the impact of phase shifting designs on IRS-NOMA," *IEEE Wireless Commun. Lett.*, vol. 9, no. 10, pp. 1596-1600, Oct. 2020.

[9] X. Yue and Y. Liu, "Performance analysis of intelligent reflecting surface assisted NOMA networks," *IEEE Trans. Wireless Commun.*, vol. 21, no. 4, pp. 2623-2636, Apr. 2022.

[10] Y. Xiu *et al.*, "Reconfigurable intelligent surfaces aided mmWave NOMA: Joint power allocation, phase shifts, and hybrid beamforming optimization," *IEEE Trans. Wireless Commun.*, vol. 20, no. 12, pp. 8393–8409, Dec. 2021.

[11] X. Li, Z. Xie, Z. Chu, V. G. Menon, S. Mumtaz, and J. Zhang, "Exploiting benefits of IRS in wireless powered NOMA networks," *IEEE Trans. Green Commun. Netw.*, vol. 6, no. 1, pp. 175–186, Mar. 2022.

[12] Z. Yang, Y. Liu, Y. Chen and N. Al-Dhahir, "Machine learning for user partitioning and phase shifters design in RIS-aided NOMA networks," *IEEE Trans. Commun.*, vol. 69, no. 11, pp. 7414-7428, Nov. 2021

[13] R. Zhong, Y. Liu, X. Mu, Y. Chen, and L. Song, "AI empowered RIS assisted NOMA networks: Deep learning or reinforcement learning?" *IEEE J. Sel. Areas Commun.*, vol. 40, no. 1, pp. 182–196, Jan. 2022.

[14] T. Shafique, H. Tabassum, and E. Hossain, "Optimization of wireless relaying with flexible UAV-borne reflecting surfaces," *IEEE Trans. Commun.*, vol. 69, no. 1, pp. 309-325, Jan. 2021.

[15] L. Yang, F. Meng, J. Zhang, M. O. Hasna, and M. D. Renzo, "On the performance of RIS-assisted dual-hop UAV communication systems," *IEEE Trans. Veh. Technol.*, vol. 69, no. 9, pp. 10385–10390, Sep. 2020.

[16] Q. Zhang, W. Saad, and M. Bennis, "Reflections in the sky: Millimeter wave communication with UAV-carried intelligent reflectors," *IEEE Global Commun. Conf. (GLOBECOM)*, Waikoloa, HI, USA, pp. 1-6, Dec. 2019.

[17] E. Bjornson, M. Matthaiou, and M. Debbah, "A new look at dual-hop relaying: Performance limits with hardware impairments," *IEEE Trans. Commun.*, vol. 61, no. 11, pp. 4512-4525, Nov. 2013.

[18] C. K. Singh and P. K. Upadhyay, "Overlay cognitive IoT-based full-duplex relaying NOMA systems with hardware imperfections," *IEEE Internet Things J.*, vol. 9, no. 9, pp. 6578-6596, May 2022.

[19] A. Al-Hourani and K. Gomez, "Modeling cellular-to-UAV path-loss for suburban environments," *IEEE Wireless Commun. Lett.*, vol. 7, no. 1, pp. 82–85, Feb. 2018.

[20] B. Talha and M. Pätzold, "On the statistical properties of double Rice channels," in *Proc. 10th Int. Symp. Wireless Pers. Multimedia Commun. (WPMC)*, Jaipur, India, pp. 517-522, Dec. 2007.